JOM, Vol. 68, No. 3, 2016
DOI: 10.1007/s11837-016-1812-6
© 2016 The Minerals, Metals & Materials Society (outside the U.S.)

Microstructure Development in Electron Beam-Melted Inconel 718 and Associated Tensile Properties

M.M. KIRKA,[1,2,7] K.A. UNOCIC,[2] N. RAGHAVAN,[3] F. MEDINA,[4] R.R. DEHOFF,[1,2] and S.S. BABU[1,5,6]

1.—Manufacturing Demonstration Facility, Oak Ridge National Laboratory, Knoxville, TN 37932, USA. 2.—Materials Science & Technology Division, Oak Ridge National Laboratory, Oak Ridge, TN 37831, USA. 3.—Bredesen Center for Interdisciplinary Research, The University of Tennessee, Knoxville, TN 37996, USA. 4.—Arcam AB, 431 37 Molndal, Sweden. 5.—Energy and Transportation Science Division, Oak Ridge National Laboratory, Oak Ridge, TN 37831, USA. 6.—Department of Mechanical, Aerospace and Biomedical Engineering, The University of Tennessee, Knoxville, TN 37996, USA. 7.—e-mail: kirkamm@ornl.gov

During the electron beam melting (EBM) process, builds occur at temperatures in excess of 800°C for nickel-base superalloys such as Inconel 718. When coupled with the temporal differences between the start and end of a build, a top-to-bottom microstructure gradient forms. Characterized in this study is a microstructure gradient and associated tensile property gradient common to all EBM Inconel 718 builds, the extent of which is dependent on build geometry and the specifics of a build's processing history. From the characteristic microstructure elements observed in EBM Inconel 718 material, the microstructure gradient can be classified into three distinct regions. Region 1 (top of a build) is comprised of a cored dendritic structure that includes carbides and Laves phase within the interdendritic regions. Region 2 is an intermediate transition zone characterized by a diffuse dendritic structure, dissolution of the Laves phase, and precipitation of δ needle networks within the interdendritic regions. The bulk structure (Region 3) is comprised of a columnar grain structure lacking dendritic characteristics with δ networks having precipitated within the grain interiors. Mechanically, at both 20°C and 650°C, the yield strength, ultimate tensile strength, and elongation at failure exhibit the general trend of increasing with increasing build height.

INTRODUCTION

Inconel 718 is an iron-nickel-base superalloy developed in the early 1960s as an advanced high-temperature, high-strength, oxidation-resistant alloy for use in gas turbine engines.[1] Inconel 718 derives its high-temperature strength from ordered γ' and γ'' precipitates that comprise nearly 30% of the alloy's volume fraction when in the peak aged condition.[2] While Inconel 718 was developed half a century ago, it is still an industry workhorse alloy, due to the wide degree of knowledge developed to generate uniform precipitate structures.[3]

Powder-bed additive manufacturing (AM) methods, such as electron beam melting (EBM) or selective laser melting (SLM) are transformative technologies which are capable of near-net shape fabrication of components with complex geometries in a broad range of alloy systems.[4] Inconel 718 fabrication by EBM or SLM is of particular interest due to the widespread use of the alloy in aerospace and other applications in which the ability to fabricate components quickly with a large degree of design flexibility is highly valued.[5–11] However, the repeated thermal exposure that occurs as a result of layer addition generates microstructures unlike those seen in traditionally processed counterparts.

Recently Tian et al.[7] studied the microstructure formation in Inconel 718 produced through direct laser melting. In their work, they showed microstructure heterogeneities within the builds at different length scales including interdendritic and interprecipitate regions. These multi-scale heterogeneities were correlated to primary solidification, remelting, and solid-state precipitation kinetics of γ''

(Published online February 12, 2016)

induced by solute segregation, as well as multiple heating and cooling cycles induced by the laser additive manufacturing process. Strondl et al.[11] studied the effect of EBM processing on Inconel 718 and observed that MC carbides preferentially align along the build direction. Further, Sames et al.[6] observed that increasing or decreasing the rate at which EBM Inconel 718 builds cool influences the monotonic tensile properties within the build plane at room temperature based upon the precipitation and coarsening of the strengthening γ''.

While much focus has been placed on developing process parameters through which alloy deposits are produced in a defect-free manner, little emphasis has been given to understanding microstructure formation and evolution in AM processed alloys.[9,12–14] Particularly, little emphasis has been given to developing the processing science and understanding to control the as-fabricated microstructure, such that a given post-process always produces the desired microstructure. The focus of this paper is to understand the microstructure formation in Inconel 718 produced through EBM and specifically the microstructure and tensile property gradients as a function of build height.

EXPERIMENTAL PROCEDURE AND METHODS

An Arcam A2 EBM machine was used to build prismatic blocks and cylinders of dimensions $100 \times 100 \times 20$ mm out of Inconel 718. The feedstock material was plasma-atomized Inconel 718 powder with a size distribution of 40–120 μm ($-100 + 325$ mesh) and nominal chemical composition given in Table I, which was manufactured by Advanced Powders and Coatings (Quebec, Canada). For the build, an Arcam A2X EBM machine equipped with EBM Control V4.1 was used with the standard linear melt theme for Inconel 718. The build began once a preheat temperature of 975°C was achieved. Throughout the build, an average beam current of 32 mA with a gun-accelerating voltage of 60 kV was used. For the build, a layer thickness of 75 μm was used.

Specimens for monotonic tensile testing were machined from the prismatic blocks perpendicular to the build direction. From each block, five specimen blanks were removed with a center-to-center spacing of 15 mm. The specimens were then machined into cylindrical dogbone geometry with a gauge diameter of 5.6 mm and gage length of 42 mm. Room-temperature monotonic tensile experiments were conducted according to ASTM E8-13a and ASTM E21-09 for tensile experiments conducted at 650°C.[15,16] In all cases, the tensile experiments were done in open air conditions and at a strain rate of 0.005 (mm/mm)/min.

Samples were sectioned using an Allied High Tech TECHCUT 5 and mounted in KonductoMet using a Buehler SimpliMet XPS1. The mounted samples were metallographically prepared using successively finer silica carbide grinding paper and given a final polish with 1 μm diamond on an Allied High Tech MetPrep 4. Chemical etching via submersion using a mixture of HCL, acetic acid, and HNO_3 (1:1:1) was used to reveal the microstructure. Microscopy was conducted using a Leica DM4000M optical microscope and a Hitachi S4800 field emission scanning electron microscope. Foils for transmission electron microscopy (TEM) were prepared

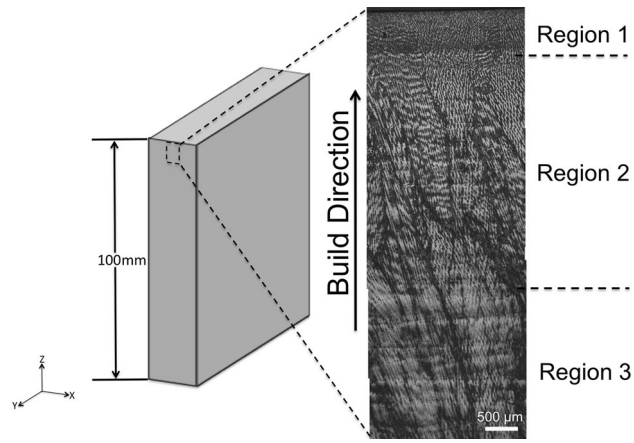

Fig. 1. OM micrograph of the microstructure gradient observed at the top of EBM Inconel 718 block with the three distinct regions discernible.

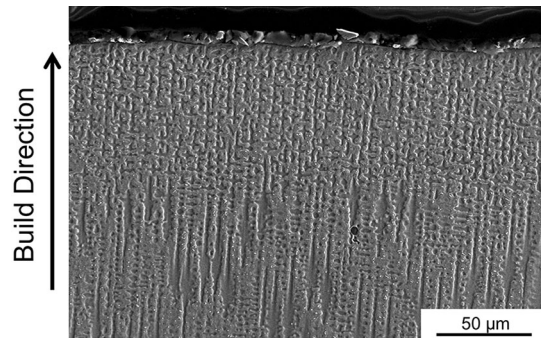

Fig. 2. SEM micrograph showing the change in the primary growth direction of the dendritic structure over the last two layers of the build.

Table I. Nominal chemical compositions of the Inconel 718 powder used in this work given in wt.%

Cr	Fe	Nb	Mo	Ti	Cu	Al	C	Ni
18.5	18.5	5	3	1	0.15	0.5	0.05	Bal

using a Hitachi NB5000 DB-FIB. TEM analysis was completed using an FEI Talos F200X field-emission 200 kV analytical TEM-STEM. Quantification of the primary dendrite arm spacing (PDAS) was determined through measuring the center-to-center distance between neighboring primary dendrite arms across a given region and averaging the measurements of that region. The γ' size was characterized through measuring the major axes of the individual γ'' found within TEM foil and averaging the values.

RESULTS AND DISCUSSION

Figure 1 shows a characteristic microstructure gradient common to all EBM Inconel 718 builds in the as-built state. However, the specific quantitative attributes are build- and process history-specific. The gradient can be thought of in similar terms to the heat-affected zones observed in welding processes where the weld microstructure varies with distance from the weld center.[17–20] From macroscopic characteristics, the gradient can be divided into three distinct regions: Region 1 – cored dendritic structure, Region 2 – diffuse dendritic structure, and Region 3 – bulk steady-state structure comprising grains lacking dendritic characteristics.

Region 1 contains the last 8–10 layers (600–750 μm) and is comprised of a dendritic structure as shown in Fig. 2. Characteristic of Region 1 is the presence of a change in the primary [001] growth direction of the dendrites spanning the last 50 μm of the build. This is attributable to changes in the orientation of the thermal gradient near the top of the melt pool.[19] Given large enough thermal gradients, heterogeneous nucleation can also occur causing an equiax cap at the top of the build as reported for laser AM processes.[19,21,22] Within the columnar region, the PDAS is 7 μm. Based on experimentally derived cooling rate/PDAS relationships, a cooling rate of 1000°C/s for the EBM Inconel 718 material can be approximated.[23–25] Comparatively, the cooling rates in laser AM processes have been reported to be 1000× greater.[7] As a result, it would be expected that EBM-induced solidification promotes a greater amount of elemental segregation than laser processes.

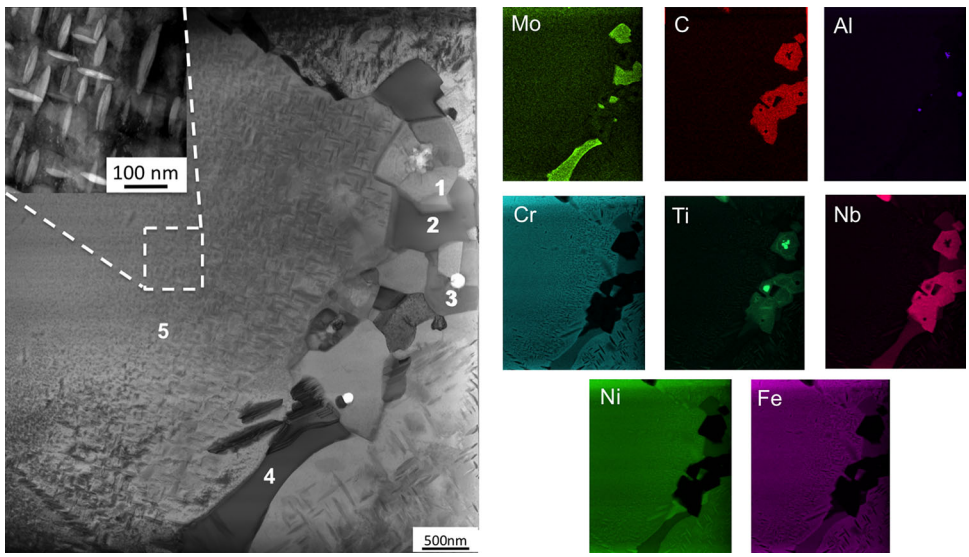

Fig. 3. TEM micrograph of the matrix and interdenritic regions as viewed within the plane of the build in the second to last layer.

Table II. Chemical compositions of the phases observed in Fig. 3 as determined through TEM EDS listed in wt.%

	Phase	Ni	Nb	Ti	Fe	Cr	Mo	Si	C
1	MC	0.43	89.91	6.01	0.15	0.62	–	–	2.73
2	Laves	42.20	22.87	0.11	13.54	11.24	9.53	0.5	–
3	MC	0.4	90.38	6.31	0.17	0.7	0.71	–	0.99
4	Laves	38.8	28.55	0.23	11.70	9.40	11.19	0.77	–
5	γ matrix	56.19	4.14	0.68	18.99	15.91	3.80	0.04	–

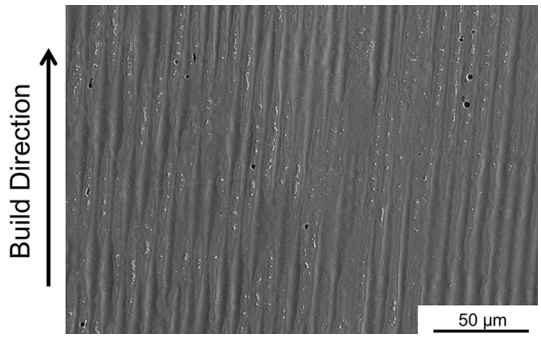

Fig. 4. SEM micrograph of the diffuse dendritic structure characteristic of Region 2.

Shown in Fig. 3 is a micrograph taken from within 100 μm of the top surface of the build. Within the matrix, γ'' with an average size of 80 nm has precipitated. Due to the short time ($\approx$180 s) between the addition of the last two layers and completion of the build in relation to the γ'' precipitation kinetics, the γ'' observed in Fig. 3 can be assumed to have precipitated after completion of the build.[2,17,26] Carbides and Laves phase of composition determined by TEM EDS (Table II) are found within the interdendritic region. The interdendritic phases are consistent with solute segregation during dendritic solidification of Inconel 718.[3,27] In comparison to Inconel 718 welds, EBM Inconel 718

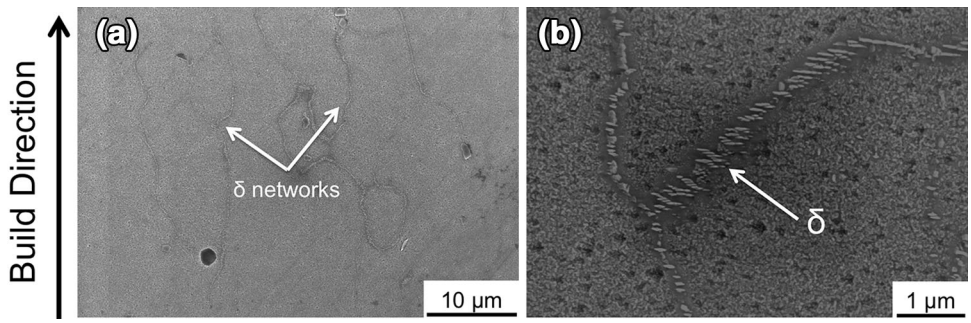

Fig. 5. SEM micrographs showing precipitation of zipper-like δ within interdendritic regions within Region 2 (a) $\times$2500 magnification, (b) $\times$20,000 magnification.

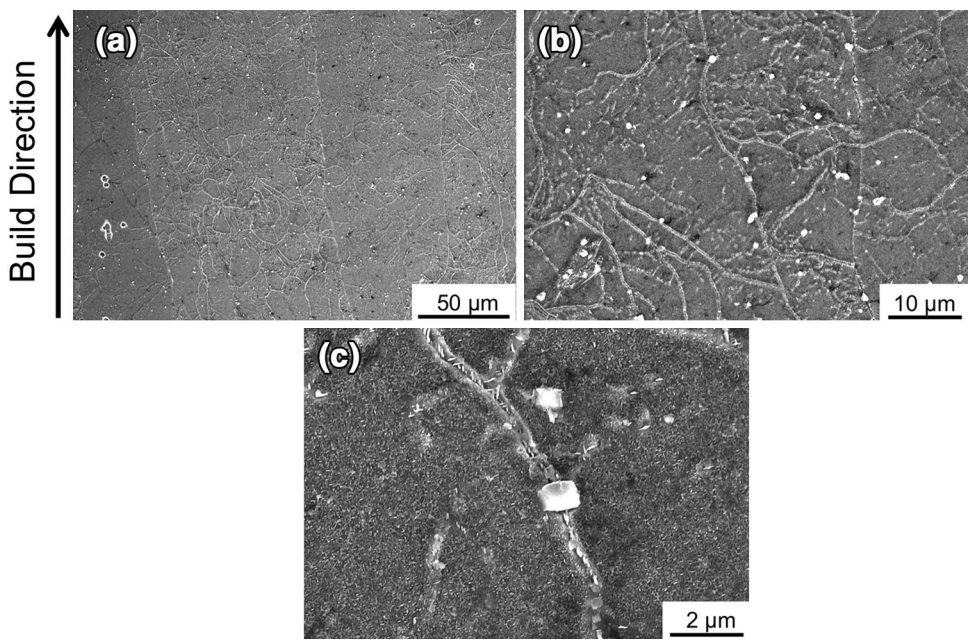

Fig. 6. SEM micrographs showing spurious δ networks spreading throughout the Inconel 718 grain structure in Region 3 (a) $\times$500 magnification, (b) $\times$2000 magnification, (c) $\times$10,000 magnification.

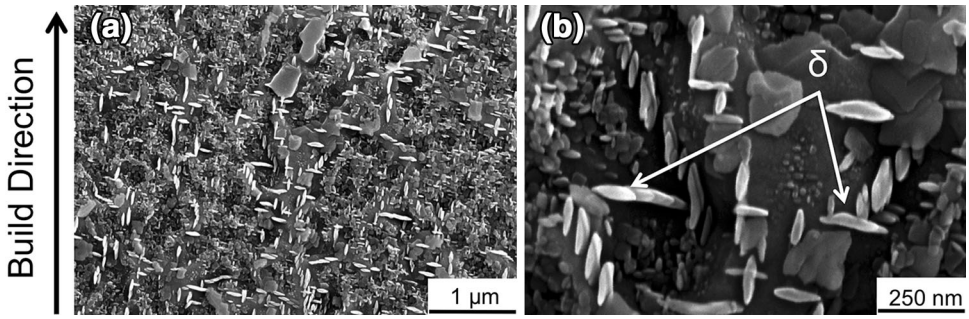

Fig. 7. SEM micrographs showing the precipitation of δ within the matrix in Region 3 separate from the δ networks shown in Fig. 6 (a) ×25,000 magnification, (b) ×100,000 magnification.

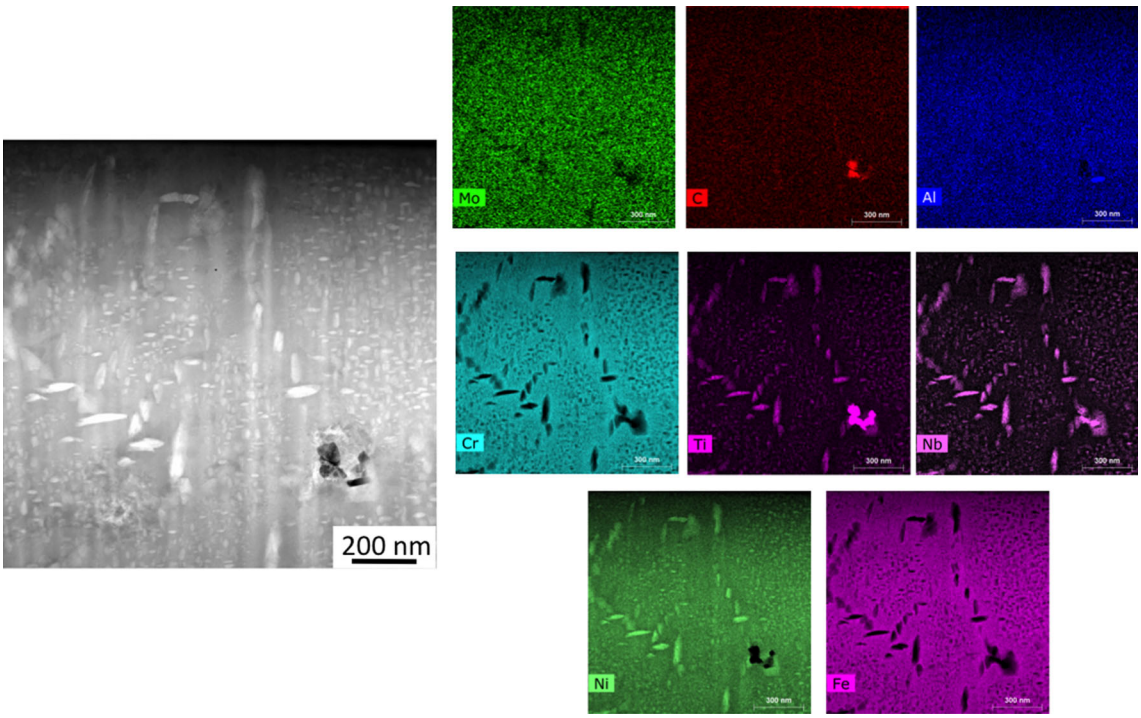

Fig. 8. TEM micrograph of intergranular δ as viewed within the plane of the build at the bottom of Region 3.

Laves phase is richer in both Nb and Mo.[17] The compositional differences can be attributed to the slower cooling rates in EBM than in welding.[17] The chemistry of the numbered precipitates is shown in Table II.

Region 2 is marked by a diffuse microstructure as shown in Figs. 1 and 4 and spans a distance of 3.5 mm. The primary dendrites coarsen from 7 μm at the transition from Regions 1 to 2 to 10 μm on average at the transition with Region 3, while the secondary dendrite arms undergo dissolution over the same vertical distance. Correspondingly, the time at temperature has the net result of decomposing the grain boundary/interdendritic Laves phase shown in Fig. 3. This is consistent with the metastable Laves phase kinetics.[3] Further, the lack of Laves can be considered beneficial, due to the phase's brittle nature and behavior as a crack initiator.[27–29] Replacing the Laves phase within the interdendritic areas are small networks of 500-nm-long δ needles as shown in Fig. 5. The formation of grain boundary δ can be attributed to the presence of concentrated niobium in the interdendritic regions[3] and most likely associated with the niobium present from the dissolution of the Laves phase.

The steady-state bulk microstructure (Region 3) starts 5 mm from the top of the build and traverses the remaining height of the build. The transition into Region 3 is marked by columnar grains lacking the characteristics of a cored dendritic structure. The observed homogenization is attributed to the short diffusion distances in the fine-scale microstructure and significant time (minimum 3 h)

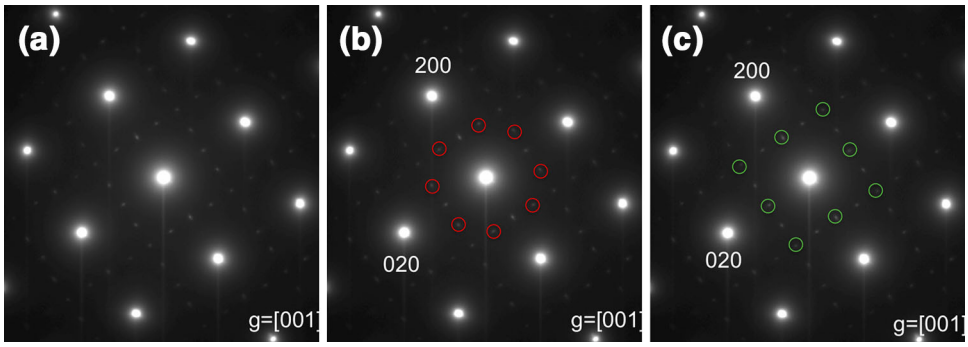

Fig. 9. (a) TEM diffraction pattern of area shown in Fig. 8 along [001] γ matrix zone axis, (b) diffraction spots unique to the three variants of γ'' (red circles) and (c) diffraction spots common to both γ' and γ'' (green circles).

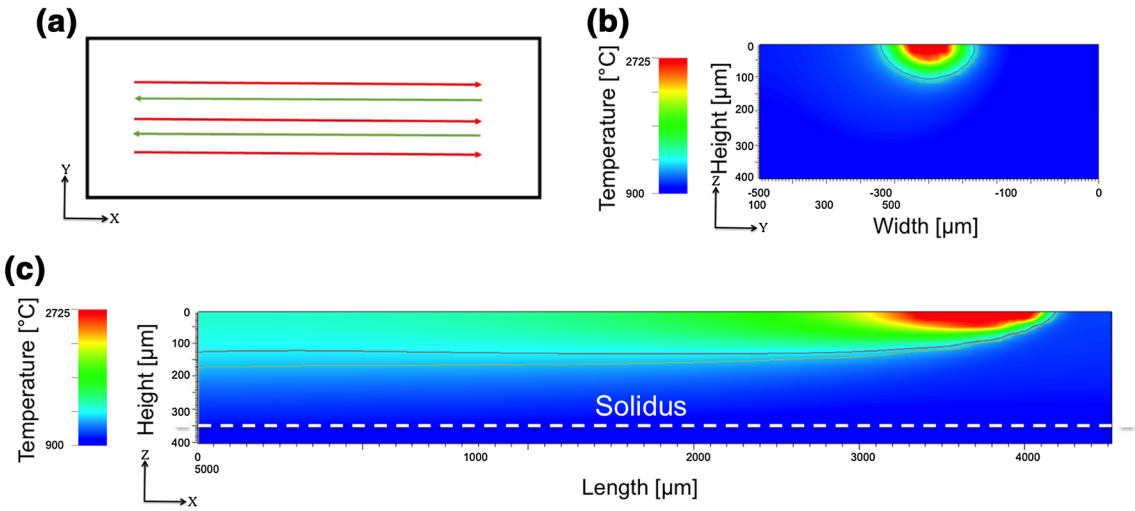

Fig. 10. TRUCHAS simulation results depicting the thermal effects associated with the addition of a 75-μm layer on already deposited material: (a) EBM raster scan, (b) thermal profile within the *Y–Z* plane, (c) thermal profile within the *X–Z* plane.

at temperature.[30] Figure 6 showsδ networks that have precipitated in a spurious manner across the columnar grains in Region 3 well away from the transition to Region 2. Within the δ networks, both globular and zipper-like δ have precipitated. Sundararaman et al. have reported similar intragranular precipitation of δ in wrought Inconel 718 at 800°C.[31] At higher temperatures δ can also precipitate directly into the austenitic γ matrix at locations of high niobium concentration as shown in Fig. 7.[31] With the precipitation of the intragranular δ, the surrounding matrix becomes denuded of γ'' (Fig. 8). Further, the γ'' size has declined to 35 nm at the bottom of the build. However, each of the three possible γ'' orientation variants ($\{100\}_{\gamma''}//\{100\}_{\gamma}$; $[001]_{\gamma''}//\langle 001\rangle_{\gamma}$) with the γ matrix remain as indicated by TEM diffraction analysis (Fig. 9).[32,33]

To understand the effects of layer addition on the existing material, the heat transfer finite-volume code TRUCHAS developed at Los Alamos National Laboratory, was used.[34] In the simulations, it was assumed that the bulk material equilibrated at 900°C, the electron beam moved in a raster pattern, and the electron beam had an effective beam diameter of 200 μm. Figure 10 shows the resultant simulated thermal profile for the addition of a new layer on the existing material. The addition of a layer results in the full melting of the uppermost two layers below the 75-μm one being added. Further, the addition of a new layer was found to result in temperatures in excess of the incipient melting temperature of Inconel 718 five layers beneath the one being added. Reported incipient temperature for Inconel 718 is in the range of 1149–1230°C; the temperature is dependent on the solidification conditions.[11,17,35] As a result, repeated incipient melting can be assumed to account for the refinement of the dendritic structure observed in the transition between Regions 1 and 2. The effect being similar to that of zone refinement in castings. Additionally, the homogenized grain structure observed in Region 3 can be associated with the materials temporal exposure to the high build temperatures and the fine scale of the microstructure.[30]

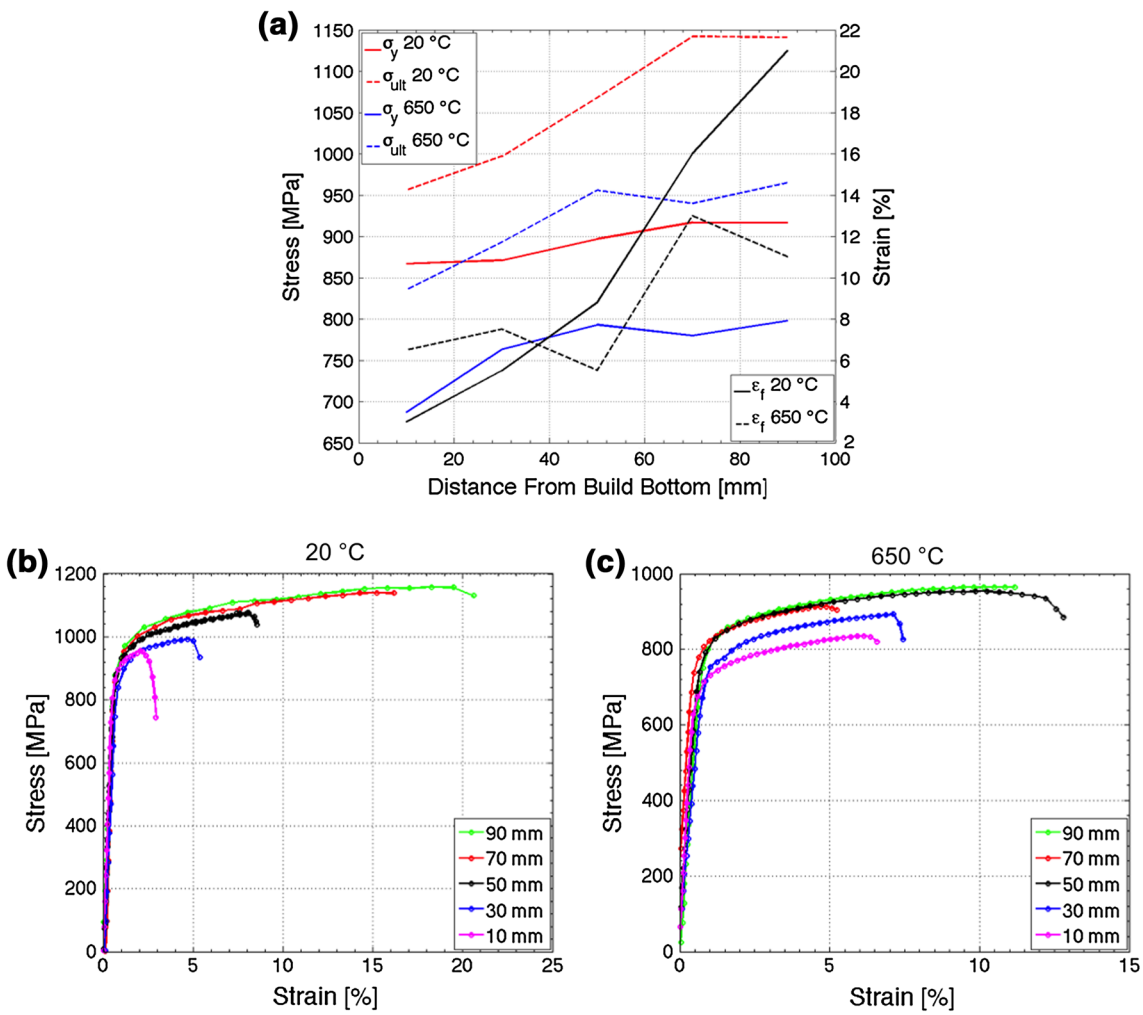

Fig. 11. Monotonic mechanical properties of EBM Inconel 718: (a) as function of build height measured at 20°C and 650°C, (b) engineering stress-strain response at 20°C, (c) engineering stress–strain response at 650°C.

Figure 11a shows the variation in the yield strength, ultimate strength, and elongation at failure as a function of build height for the material tested within the build plane. The corresponding stress–strain curves are shown in Fig. 11b and c for the room-temperature (20°C) and high-temperature (650°C) exposure. As seen, the yield and ultimate stress exhibit a height dependence starting 30 mm below the top of the build. Additionally, the elongation at failure exhibits the general trends of progressively declining with increasing distance from the top surface of the build. Comparatively, the yield and tensile strengths for the as-built EBM Inconel 718 are both 30% less on average than wrought Inconel 718 in the peak-aged state.[36]

From the observed mechanical property gradient, Regions 1 and 2 of the microstructure gradient can be considered to have minimal influence on the tensile behavior of the as-built material. This can be attributed to the relative lack of δ in Regions 1 and 2. The progressive decline of the monotonic properties at distances greater than 30 mm below the top of the build can be attributed to the increasing amounts of precipitated δ at the cost of the strengthening γ'' as shown in Figs. 6 and 7. Mechanically, the δ phases is largely considered detrimental in Inconel 718 due to the brittle nature of the phase.[2,37–39] Additionally, as the distance from the top of the build increases, the remaining γ'' increasingly coarsens according to Oswald ripening kinetics.[39] This has the undesired effect of over-aging the material and influences whether the γ'' is sheared or by-passed by dislocations during mechanical deformation.[2,40,41] As will be discussed in a companion paper, a post-processing heat treatment is required to homogenize the material and eliminate the microstructure/ mechanical property gradient.

CONCLUSION

The effects of the EBM build process on the microstructure and mechanical behavior of Inconel 718 have been investigated. While these effects were considered in the context of a specific build

geometry and process history, the general trends and observations are common to all EBM Inconel 718 builds. The findings of this work can be generalized as follows for all EBM Inconel 718 builds:

- EBM Inconel 718 builds in the as-built state exhibit a microstructure gradient along the build direction. The microstructure gradient is classified into three distinct regions based on characteristic observations:

  Region 1: The last layers of the build solidify in a dendritic manner with a change in the primary growth direction occurring within the last two layers. Within the dendritic cores γ'' has precipitated, while carbides and Laves phase have precipitated within the interdendritic regions.
  Region 2: An intermediate transition zone which is characterized by a diffuse dendritic structure largely lacking secondary dendrite arms and the interdendritic Laves phase observed in Region 1. In place of the interdendritic Laves, networks of fine δ needle have precipitated.
  Region 3: Bulk grain structure consisting of columnar grains lacking characteristics of dendritic segregation. Networks of δ consisting of both globular and small needle-like δ morphologies precipitated across the matrix. The presence of δ within the matrix corresponds to a decrease in volume fraction of the strengthening γ'' precipitates.

- Computational simulations of layer addition revealed that the addition of a layer resulted in the full or partial remelting of solid material approximately 5 layers beneath the one being added. This continual melting, solidification, and remelting sequence causes the diffuse dendritic structure observed in Region 2. Additionally, the homogenized structure observed in Region 3 is attributed to the exposure of the material to the high build temperatures.
- As a function of build height, the in-plane monotonic properties of the build exhibit a gradient similar to the microstructure but on a larger length scale. With increasing distance from the bottom of the build, the yield and tensile strength and elongation progressively increase. The mechanical property gradient is associated with the increased precipitation of δ and corresponding decomposition of the strengthening γ'' with increased distance from the top of the build.

ACKNOWLEDGEMENTS

This research is sponsored by the US Department of Energy, Office of Energy Efficiency and Renewable Energy, Advanced Manufacturing Office, under Contract DE-AC05-00OR22725 with UT-Battelle, LLC. The United States Government retains, and the publisher, by accepting the article for publication, acknowledges that the United States Government retains, a non-exclusive, paid-up, irrevocable, worldwide license to publish or reproduce the published form of this manuscript, or allow others to do so, for United States Government purposes. This research was performed, in part, using instrumentation provided by the Department of Energy, Office of Nuclear Energy, Fuel Cycle R&D Program and the Nuclear Science User Facilities.

REFERENCES

1. H.J. Wagner, and A.M. Hal, Tech. Rep. (Battelle Memorial Institue, Columbus, 1965).
2. C. Sims, *The Superalloys* (Wiley, New York, 1972).
3. J.F. Radavich, in *Superalloy 718: Metallurgy and Applications*, ed. by E. Loria (Minerals, Metals & Materials Society, USA, 1989), pp. 229–240.
4. I. Gibson, D. Rosen, and B. Stucker, *Additive Manufacturing Technologies* (Springer, New York, 2010).
5. H.E. Helmer, C. Körner, and R.F. Singer, *J. Mater. Res.* 29, 1987 (2014).
6. W. Sames, K. Unocic, R. Dehoff, T. Lolla, and S. Babu, *J. Mater. Res.* 29, 1920 (2014).
7. Y. Tian, D. McAllister, H. Colijn, M. Mills, D. Farson, M. Nordin, and S. Babu, *Metall. Mater. Trans. A* 45, 4470 (2014).
8. K. Unocic, L. Kolbus, R. Dehoff, S. Dryepondt, and B. Pint, *Corrosion* (NACE International, USA, 2014).
9. K. Amato, S. Gaytan, L. Murr, E. Martinez, P. Shindo, J. Hernandez, S. Collins, and F. Medina, *Acta Mater.* 60, 2229 (2012).
10. Z. Wang, K. Guan, M. Gao, X. Li, X. Chen, and X. Zeng, *J. Alloys Compd.* 513, 518 (2012).
11. A. Strondl, R. Fischer, G. Frommeyer, and A. Schneider, *Mater. Sci. Eng. A* 480, 138 (2008).
12. L. Carter, M. Attallah, and R. Reed, in *Superalloys 2012*, ed. by E. Huron, R. Reed, M. Hardy, M. Mills, R. Montero, P. Portella, and J. Telesman (Wiley, New York, 2012), p. 577.
13. L. Murr, E. Martinez, X. Pan, S. Gaytan, J. Castro, C. Terrazas, F. Medina, R. Wicker, and D. Abbott, *Acta Mater.* 61, 4289 (2013).
14. L. Murr, E. Martinez, S. Gaytan, D. Ramirez, B. Machado, P. Shindo, J. Martinez, F. Medina, J. Wooten, D. Ciscel, U. Ackelid, and R. Wicker, *Metall. Mater. Trans. A* 42, 3491 (2011).
15. ASTM E08–13a, Standard Test Methods for Tension Testing of Metallic Mater. Tech. Rep. (ASTM International, 2013).
16. ASTM E21–09, Standard Test Methods for Elevated Temperature Tension Tests of Metallic Mater. Tech. Rep. (ASTM International, 2009).
17. R.G. Thompson, and S. Genculc, *Weld. Res. Supp.* 337, (1983).
18. R. Thompson, *JOM* 40, 44 (1988).
19. S. David, S. Babu, and J. Vitek, *JOM* 55, 14 (2003).
20. S. Babu, M. Miller, J. Vitek, and S. David, *Acta Mater.* 49, 4149 (2001).
21. M. Gäumann, C. Bezençon, P. Canalis, and W. Kurz, *Acta Mater.* 49, 1051 (2001).
22. J.D. Hunt, *Mater. Sci. Eng.* 65, 75 (1984).
23. J. Tien, and T. Caulfield, *Superalloys, Supercomposites, and Superceramics* (Academic, New York, 1989).
24. Y. Zhang, Z. Li, P. Nie, and Y. Wu, *Metall. Mater. Trans. A* 44, 5513 (2013).
25. W. Kurz, B. Giovanola, and R. Trivedi, *Acta Metall.* 34, 823 (1986).
26. A. Devaux, L. Nazé, R. Molins, A. Pineau, A. Organista, J. Guédou, J. Uginet, and P. Héritier, *Mater. Sci. Eng. A* 486, 117 (2008).
27. G. Bouse, in *Superalloys 718, 625 and Various Derivatives*, 1989, ed. by E. Loria, p. 69.

28. J. Schirra, R. Caless, and R. Hatala, in *Superalloys 718, 625 and Various Derivatives*, 1989, ed. by E. Loria, p. 375.
29. G. Sjoberg, N. Ingesten, and R. Carlson, in *Superalloys 718, 625 and Various Derivatives*, 1989, ed. by E. Loria, p. 603.
30. X. Liang, R. Zhang, Y. Yang, and Y. Han, in *Superalloys 718, 625, 706 and Various Derivatives*, 1994, ed. by E. Loria, p. 947.
31. M. Sundararaman, P. Mukhopadhyay, and S. Banerjee, *Mater. Trans. A* 19, 453 (1988).
32. J.M. Oblak, D.F. Paulonis, and D.S. Duvall, *Metall. Mater. Trans.* 5, 143 (1974).
33. M. Sundararaman, and P. Mukhopadhyay, *Mater. Char.* 31, 191 (1993).
34. D.A. Korzekwa, *Int. J. Cast Metals Res.* 22, 187 (2009).
35. W. Cao, R. Kennedy, and M. Willis. in *Superalloys 718, 625 and Various Derivatives*, 1991, ed. by E. Loria, p. 147.
36. G.A. Rao, M. Srinivas, and D. Sarma, *Mater. Sci. Technol.* 20, 1161 (2004).
37. H. Zhang, S. Zhang, M. Cheng, and Z. Li, *Mater. Char.* 61, 49 (2010).
38. S. Azadian, L.-Y. Wei, and R. Warren, *Mater. Char.* 53, 7 (2004).
39. S. Wlodek, and D. Field, in *Superalloys 718, 625, 706 and Various Derivatives*, 1994, ed. by E. Loria, p. 659.
40. M.C. Chaturvedi, and Y.-F. Han, *Metal Sci.* 17, 145 (1983).
41. A. Argon, *Strengthening Mechanisms in Crystal Plasticity* (Oxford University Press, New York, 2007), pp. 113–144.